Research article

Raghu Dharmavarapu*, Ken-ichi Izumi, Ikufumi Katayama, Soon Hock Ng, Jitraporn Vongsvivut, Mark J. Tobin, Aleksandr Kuchmizhak, Yoshiaki Nishijima, Shanti Bhattacharya* and Saulius Juodkazis*

Dielectric cross-shaped-resonator-based metasurface for vortex beam generation at mid-IR and THz wavelengths

https://doi.org/10.1515/nanoph-2019-0112
Received April 9, 2019; revised May 30, 2019; accepted June 1, 2019

Abstract: Metasurfaces are engineered thin surfaces comprising two-dimensional (2D) arrays of sub-wavelength-spaced and sub-wavelength-sized resonators. Metasurfaces can locally manipulate the amplitude, phase, and polarization of light with high spatial resolution. In this paper, we report numerical and experimental results of a vortex-beam-generating metasurface fabricated specifically for infrared (IR) and terahertz (THz) wavelengths. The designed metasurface consists of a 2D array of dielectric cross-shaped resonators with spatially varying length, thereby providing the desired spatially varying phase shift to the incident light. The metasurface was found to be insensitive to the polarization of the incident light. The dimensions of the cross-resonators were calculated using rigorous finite-difference time-domain analysis. The spectral scalability via physical scaling of the meta-resonators is demonstrated using two vortex-generating optical elements operating at 8.8 μm (IR) and 0.78 THz. The vortex beam generated in the mid-IR spectral range was imaged using a Fourier transform IR (FTIR) imaging miscroscope equipped with a focal plane array detector. This design could be used for efficient wavefront shaping and various optical imaging applications in the mid-IR spectral range, where polarization insensitivity is desired.

Keywords: metasurface; vortex beam; mid-infrared; terahertz; micro-optics; IR imaging.

***Corresponding authors: Raghu Dharmavarapu,** Centre for NEMS and Nanophotonics (CNNP), Department of Electrical Engineering, Indian Institute of Technology Madras, Chennai 600036, India; Centre for Micro-Photonics, Faculty of Science, Engineering and Technology, Swinburne University of Technology, Hawthorn, Victoria 3122, Australia; and Melbourne Centre for Nanofabrication, ANFF, 151 Wellington Road, Clayton, Victoria 3168, Australia, e-mail: raghu.d@ee.iitm.ac.in. https://orcid.org/0000-0002-8263-7966; **Shanti Bhattacharya,** Centre for NEMS and Nanophotonics (CNNP), Department of Electrical Engineering, Indian Institute of Technology Madras, Chennai 600036, India, e-mail: shantib@iitm.ac.in. https://orcid.org/0000-0002-1213-5514; and **Saulius Juodkazis,** Centre for Micro-Photonics, Faculty of Science, Engineering and Technology, Swinburne University of Technology, Hawthorn, Victoria 3122, Australia; Melbourne Centre for Nanofabrication, ANFF, 151 Wellington Road, Clayton, Victoria 3168, Australia; Institute of Advanced Sciences, Yokohama National University, 79-5 Tokiwadai, Hodogaya-ku, Yokohama 240-8501, Japan; and Tokyo Tech World Research Hub Initiative (WRHI), School of Materials and Chemical Technology, Tokyo Institute of Technology, 2-12-1 Ookayama, Meguro-ku, Tokyo 152-8550, Japan, e-mail: sjuodkazis@swin.edu.au. https://orcid.org/0000-0003-3542-3874

Ken-ichi Izumi and Ikufumi Katayama: Physics Department, Yokohama National University, 79-5 Tokiwadai, Hodogaya-ku, Yokohama 240-8501, Japan

Soon Hock Ng: Centre for Micro-Photonics, Faculty of Science, Engineering and Technology, Swinburne University of Technology, Hawthorn, Victoria 3122, Australia; and Melbourne Centre for Nanofabrication, ANFF, 151 Wellington Road, Clayton, Victoria 3168, Australia

Jitraporn Vongsvivut and Mark J. Tobin: Infrared Microspectroscopy Beamline, Australian Synchrotron, Clayton, Victoria 3168, Australia

Aleksandr Kuchmizhak: Institute of Automation and Control Processes, Far Eastern Branch, Russian Academy of Sciences, Vladivostok 690041, Russia; and Far Eastern Federal University, Vladivostok 690090, Russia

Yoshiaki Nishijima: Department of Electrical and Computer Engineering, Graduate School of Engineering, Yokohama National University, 79-5 Tokiwadai, Hodogaya-ku, Yokohama 240-8501, Japan; and Institute of Advanced Sciences, Yokohama National University, 79-5 Tokiwadai, Hodogaya-ku, Yokohama 240-8501, Japan

1 Introduction

Optical elements to be used in the infrared (IR) and terahertz (THz) spectral ranges with wavelengths spanning from tens of micrometers to sub-millimeters and polarization optical elements based on refraction become nonpractical because of the shortage of highly transparent materials in these wavelength regimes. In addition, their fabrication can often be challenging for high-aspect-ratio patterns over large macroscopic areas. IR and THz radiations have been used and applied extensively by the optical research and development community in the past decades. While THz technology has gained increasing demand for applications in the sensing and noninvasive imaging fields [1–3], IR-based techniques have been established as a molecular characterization tool for a wide range of applications in microstructural analysis, spectroscopy, and imaging [4, 5].

Several methods have been proposed to fabricate basic optical elements for these wavelengths, such as refractive and diffractive lenses, polarizers, and beam splitters [6, 7]. Recently, a three-dimensional (3D) printing technique was employed to fabricate nonconventional diffractive optical elements to generate complex light beams such as Bessel, Airy, and vortex beams in the THz and IR wavelengths [8–10]. Although 3D printing is often considered to be a good solution for generating custom light beams, this approach is still limited for applications that require high fabrication throughput due to the direct write character. There is considerably less work on THz and IR complex light generation despite their huge potential applications. Diffractive optical elements (DOEs) could be considered a solution because they reduce the volume that should be 3D-printed. However, the efficiency of DOEs is significantly low, leading to a major limitation, especially for applications in the THz spectral window.

Laguerre Gaussian beams, also known as vortex beams, are interesting complex beams in optics, which possess helical wavefronts and an on-axis phase singularity [11, 12]. In addition, composite vortex beams possess a self-healing property within the Rayleigh range [13]. Owing to these interesting properties, vortex beams have been used in many applications, such as optical manipulation of microparticles [14, 15], fiber-optic communication [16], and stimulated emission depletion (STED) microscopy [17]. Currently, the most popular techniques to generate these beams in the visible wavelengths include computer-generated holograms [18], spatial light modulators [19], spiral phase plates (SPPs) [20], and so on. In 2012, Genevet et al. employed a V-shaped-antenna-based metasurface [21] to build a vortex-generating SPP in the IR spectral region. A year later, the same design concept was extended to the THz region and used to fabricate vortex generators [22]; also a modified version of the antenna was proposed to generate vortex beams in the THz region [23]. Geometric metasurfaces, which work on the Pancharatnam-Berry phase phenomenon, are used to generate both scalar [24] and vector [25] vortex beams. Recently, polarization-sensitive generation and modulation [26] of orbital angular momentum (OAM) beams was reported using dielectric metasurfaces based on silicon fin structures. Metasurfaces have recently become a platform to realize and apply the optical spin-Hall effect [27]. Metasurfaces can be built using several types of meta-atoms, such as V-shaped antennas [28], cylindrical disks [29], or nano-fin structures [30].

In this work, we have developed a vortex beam generator for the mid-IR spectral range (8.8 μm), using cross-shaped resonators [31], which can support both Mie-type electric and magnetic dipole resonances to realize phase manipulation and to completely suppress reflection losses. The idea behind choosing this wavelength was to use the generated vortex beam to measure the absorbance of secondary protein structures such as the β-sheets in silk, which also lies at in the same wavelength region [32–35]. The generated vortex beam was captured, for the first time, using a Fourier transform infrared (FTIR) imaging microscope with a focal plane array (FPA) detector. To show the versatility and scalability of this design, we scaled the IR design and generated a vortex beam of charge 1 at 0.78 THz. The transmission response of both s- and p-polarizations showed a polarization insensitivity for this design. Finite-difference time-domain (FDTD) simulation, fabrication, and optical characterization results are presented to support the experimental results.

2 Results and discussion

2.1 Design of the unit cell

In this section, we discuss the design parameters and dimensions of silicon cross-resonators to achieve high transmission and 0–2π phase response for full wavefront control. A schematic of the silicon cross-resonator is shown in the inset of Figure 1B. Silicon was chosen because of its high relative permittivity of $\varepsilon_r = 13.5$ and its low loss in the THz regime. The design frequency is chosen to be 34 THz, which lies in one of the absorption bands of silk in the IR spectral range. The following cross-resonator dimensions were optimized to get maximum transmission and 2π

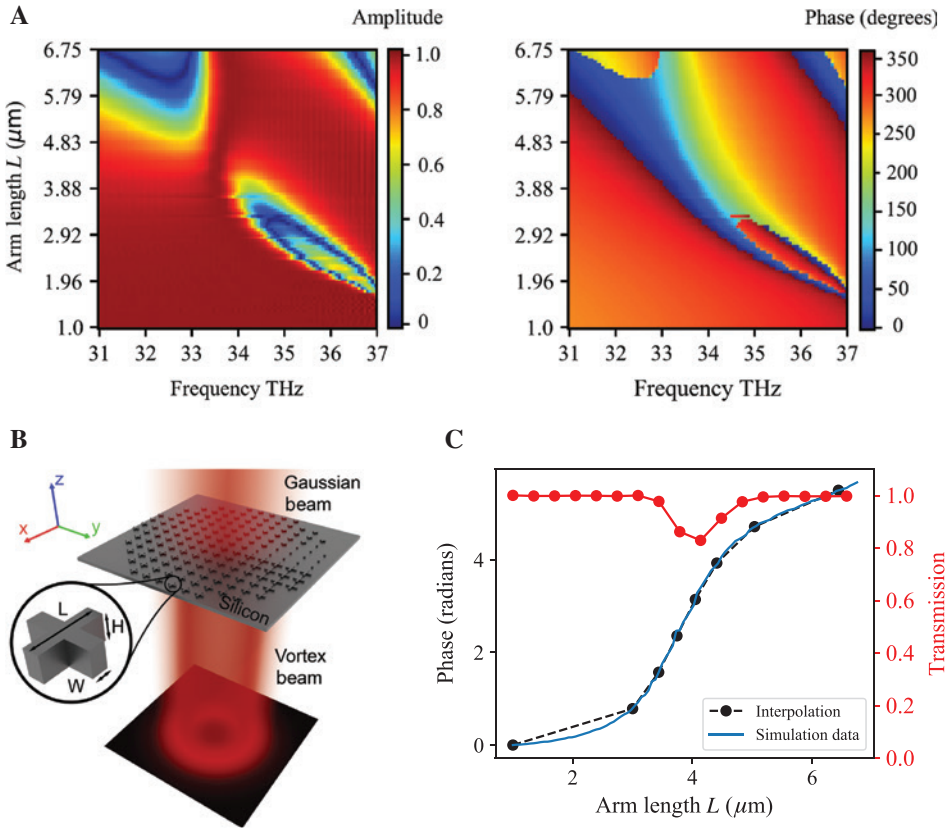

Figure 1: Meta-atom design summary and schematic layout of the Spiral Phase Plate.
(A) Simulated transmission amplitudes and the corresponding transmission phases as a function of arm length L, over the frequency range 31–37 THz. Spectral position near 34 THz was selected for design of vortex generator because of the constant transmission amplitude and possibility of 2π phase control. (B) Schematic of the vortex generator layout and silicon cross meta-atom in the inset. (C) Look-up table for IR cross-resonators. The length L of the cross-arm is varied from 1 to 6.5 μm to achieve 0–2π transmission for the IR design.

phase coverage at the chosen operational frequency. The 2π phase coverage is achieved by changing the length of the resonator from 1.25 to 6.5 μm. The width, height, and lattice constant of the unit cell were fixed at 1, 1.85, and 7.25 μm, respectively.

We considered the electromagnetic response of one resonator with periodic boundary conditions, as the spacing between the resonators was sub-wavelength, which allowed very low coupling between the adjacent resonators. Each resonator can support electric and magnetic resonances when the dimensions become comparable to the wavelength of the incident light [36]. High transmission can be achieved by tuning the dimensions such that the two resonances overlap spectrally and cancel out the backscattered light. In our simulations, the refractive index model of silicon is fitted to Palik data, and the incident wave is assumed to be a plane wave propagating along the z-axis with the electric field along the x-direction. The transmission amplitude and phase are extracted from the S21 parameter of the FDTD simulation. The FDTD-extracted electric field amplitude and phase data for different cross-lengths (1.25–6.5 μm) and operating frequencies (31–37 THz) are shown in Figure 1A. The plot in Figure 1C shows the variation of transmission amplitude and phase with respect to changing cross-lengths from 1.25 to 6.5 μm at the desired frequency of 34 THz ($\lambda = 8.8$ μm).

For the THz vortex generator we chose 0.78 THz as the operating frequency. This corresponds to a wavelength of 410 μm. This wavelength was selected as the band close to the coherent synchrotron radiation (CSR) at 0.3–0.4 THz. CSR is a unique and the highest brightness radiation source in the IR beamline at the Australian synchrotron facility, which can benefit from a set of optical elements to control the polarization, intensity, and wavefront. We used linear scaling to find the desired starting dimensions for the THz metasurface. The wavelength scaling factor was 46.5, which was calculated by taking the ratio of the two wavelengths. We found the maximum length for the cross-resonator to be approximately 300 μm by applying

the same scaling factor to the length of the cross-resonator. By using further FDTD optimization, we narrowed down the desired length range to 180–275 µm to achieve 0–2π phase coverage at 0.78 THz. The width, height, and lattice constant of the cross were fixed at 70, 150, and 380 µm, respectively.

2.2 Mid-IR vortex generator

A metasurface for vortex beam generation at mid-IR wavelengths is constructed as follows. The phase function of the vortex generator is given by the helical function

$$\Phi(x, y) = l \tan^{-1}(y/x), \tag{1}$$

where (x, y) are the coordinates in the metasurface plane, and l is the topological charge of the vortex beam. The continuous phase profile of the vortex generator given in Eq. (1) is discretized to eight phase levels, and eight cross-dimensions with nearly equal phase steps of $\pi/4$ to cover the full 2π range are selected from the look-up table plot of Figure 1C. It can be seen that all the resonators have high transmission with a mean variation of only 5%. The schematic of the vortex generator is shown in Figure 1B.

To gain intuitive insight into the phase-tuning phenomenon of the cross-resonator, a simple analytical model [37] is presented here. Each of the cross-resonators can be considered a coupled electric and magnetic dipole excited by an incident electromagnetic wave. The far-field electric field of the metasurface is the sum of the incident field and the electric and magnetic dipole radiation coming from these individual cross-resonators. Therefore, the transmission coefficient of each resonator can be written as

$$t(\omega) = 1 + \frac{2j\gamma_e\omega_e}{\omega_e^2 - \omega^2 - 2j\gamma_e\omega_e} + \frac{2j\gamma_m\omega_m}{\omega_m^2 - \omega^2 - 2j\gamma_m\omega_m}, \tag{2}$$

where ω is the frequency of the incident beam, ω_e and ω_m are the electric and magnetic resonance frequencies, and γ_e and γ_m are the damping factors of the electric and magnetic dipoles. Figure 2A shows the transmission phase and amplitude simulated using FDTD (red curve) and the curve fit to the analytical model given in Eq. (2) for the cross-resonator with an arm length of 3 µm. For this cross-resonator, we have extracted the electric and magnetic resonance frequencies ω_e, ω_m and the damping factors γ_e, γ_m to be 35.0, 35.1 THz and 2.13, 0.72, respectively, using curve fitting. The difference between the analytical model and FDTD data can be attributed to the finite mesh settings of the FDTD solver. Figure 2B shows the maximum variation in the transmission amplitude (ΔT) and phase coverage ($\Delta\Phi$) among the eight chosen cross-resonators over the wavelength range 8.3–9.5 µm. Even though the resonators provide nearly the desired 2π (gradually decreasing) phase coverage over the entire frequency band, all the cross-resonators at a specific frequency do not have the same transmission, which can be clearly seen from the dip in Figure 2B. If we consider that a 20% variation in transmission among the resonators is acceptable, we can use this design over a bandwidth of ~170 nm, around 8.85 µm.

We used a 500-µm-thick silicon wafer to fabricate the IR vortex generator. The device was fabricated using electron beam lithography (Vistec EBPG) followed by anisotropic dry etching using the standard Bosch process, with the photoresist acting as the etch mask. The etching recipe was optimized to get the desired cross-height of 1.85 µm. An SEM image of the fabricated vortex plate is shown in Figure 3A, where the inset was captured at higher magnification to show a single cross meta-atom.

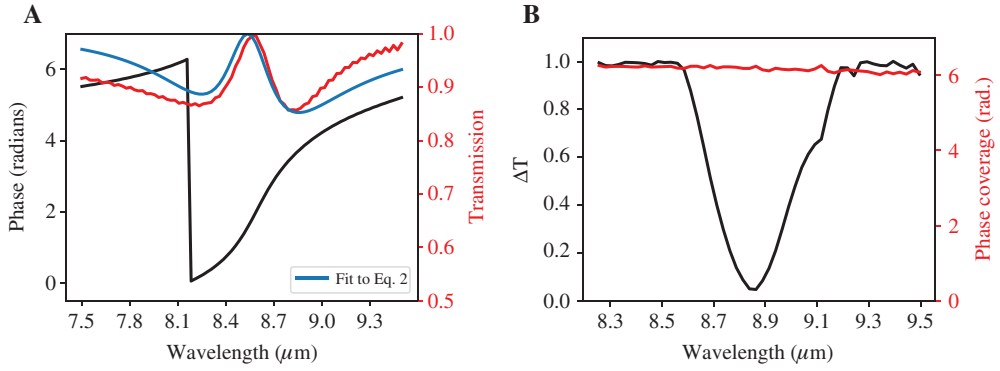

Figure 2: Transmission characteristics of single meta atom and bandwidth of the meta device.
(A) FDTD-simulated amplitude and phase for a cross-resonator with arm length $L = 3$ µm; curve-fitting to Eq. (2) is plotted by the blue line. (B) Maximum change in the transmission ΔT and phase coverage among the eight chosen cross-resonators.

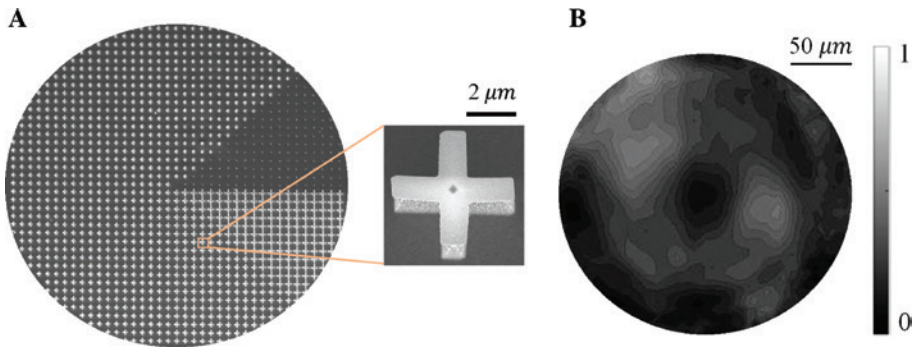

Figure 3: SEM image of the fabricated SPP and vortex beam captured using FPA detector.
(A) SEM image of meta SPP for $l = +1$ topological charge. The inset shows the single building block. (B) Vortex beam image captured on the 64 × 64 pixel FPA detector.

2.2.1 FPA-FTIR imaging of the vortex generator

The IR images of the vortex beam were acquired with an offline FPA-FTIR microspectroscopic instrument at the Australian Synchrotron Infrared Microspectroscopy (IRM) beamline. The system consisted of a Bruker Hyperion 3000 FTIR microscope (Bruker Optik GmbH, Ettlingen, Germany), equipped with a liquid-N_2-cooled 64 × 64 element FPA detector and a matching 15× objective and condenser (NA = 0.40), which was coupled to a Vertex 70 FTIR spectrometer (Bruker Optik GmbH, Ettlingen, Germany) containing an internal thermal (Globar) IR source.

FPA-FTIR images were collected in the transmission mode in the 4000–800 cm^{-1} spectral region as a single FTIR image covering a sampling area of 180 × 180 μm^2. Each FTIR spectral image consisted of a 64 × 64 array of spectra, resulting from each square of the detector on the 64 × 64 element FPA array. As a consequence, a single spectrum contained in an FTIR image represented approximately 2.8 × 2.8 μm^2 area on the sample plane.

For each image, high-quality FTIR spectral images were collected at 4 cm^{-1} resolution, with 128 co-added scans, Blackman-Harris three-term apodization, power-spectrum phase correction, and a zero-filling factor of 2 using the OPUS 7.2 imaging software (Bruker). Background measurements were taken using the same acquisition parameters prior to the sample spectral images, by focusing on a clean surface area of the substrate without the vortex pattern. All spectra were analyzed using the OPUS v7.2 software, by integrating the area under the narrow spectral range around 1136 cm^{-1} ($\lambda = 8.8$ μm). Figure 3B shows the vortex beam captured on the FPA detector. The low image quality can be attributed to the use of only eight steps in the SPP and the lower resolution of the FPA sensor itself. A higher number of phase steps would improve the contrast of the vortex intensity profile.

2.3 THz vortex generator

We designed the SPP with a diameter of 1.2 cm consisting of eight phase levels in its eight octants. Each of the octants contained an array of cross-resonators such that the phase varied from 0 to 2π azimuthally across vortex generator. Such an optical element has dimensions useful for a range of applications in THz experiments. The FDTD simulation results of the transmitted phase and electric field amplitude are shown in Figure 4A and B, respectively. The designed spiral phase was found to indeed follow the required 2π azimuthal span. We could experimentally show the high transmission and polarization independence for this metasurface. However, we could not image the vortex generator in a raster scan mode, as our experimental setup was not capable of such mapping.

To simulate the SPP and the doughnut intensity pattern of the vortex generator, we created its GDSII layout (schematic shown in Figure 1B) using an in-house-developed software MetaOptics [38]. MetaOptics uses FDTD transmission phase versus varying dimensions of a meta-atom and creates GDSII layouts of any phase distribution by placing a meta-atom that gives the desired transmission phase at that pixel of the phase mask. The generated GDSII file is loaded in the Lumerical FDTD solver for simulation. The corresponding simulated phase and doughnut intensity pattern are shown in Figure 4A and B.

2.3.1 Fabrication of vortex generator

A 300-μm-thick intrinsic silicon wafer was used for the fabrication of the optical metasurface element. The device was fabricated using photolithography followed by reactive ion etching (RIE). The mask for photolithography was fabricated using the Intelligent Micropatterning SF100 XPRESS direct writing system. To achieve a resist layer

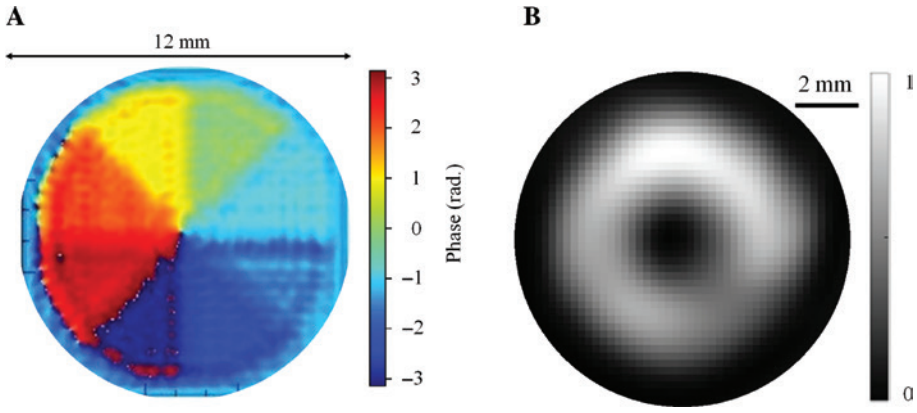

Figure 4: FDTD simulation of transmission phase and intensity of the SPP.
(A) Azimuthal phase variation from 0 to 2π and (B) electric field intensity $|E|^2$ distribution of the THz vortex beam generator. The simulation frequency is 0.78 THz.

of >10 μm thickness, ths AZ4562 photoresist was spin-coated at 2000 rpm. The large thickness was needed to obtain a high etch depth of 150 μm by RIE (as the resist acts as a sacrificial mask during this process). The resist was exposed at a dose of 485 μJ/cm^2, and then developed in AZ726 MIF for 5 min. The standard Bosch process was used to etch silicon for the required pattern of high aspect ratio. A photograph of the fabricated metadevice and the optical profilometer measurement are shown in Figure 5A and B, respectively. The required depth of 150 μm was achieved after 90 min of plasma etching.

2.3.2 Characterization by time-domain spectroscopy

Terahertz time-domain spectroscopy (THz-TDS) was used to characterize the performance of the THz vortex generator shown in Figure 5A. Terahertz transmission spectra of the microstructures were measured using a home-made terahertz time-domain spectrometer using a 10-fs Ti:sapphire oscillator with the repetition rate of 80 MHz and output power of 300 mW. The terahertz waves were generated and detected by low-temperature-grown GaAs photoconducting antennae used in the reflection geometry [39]. The THz spectrum spans a broad bandwidth from 0.2 to 15 THz with a dip at 8 THz. The transmittance of the samples were characterized by the ratio of the spectrum of the transmitted THz wave through the sample to that through the bare silicon substrate of the same thickness. We measured the transmittance at several different positions on the vortex generators. The positions of the incident THz waves were confirmed by the residual of the pump laser reflected from the surface of the generation photoconducting antenna. This guide light was filtered by an additional silicon plate during the measurement. The system was purged with nitrogen to avoid water vapor absorption.

Almost identical E-field transients were observed in transmission at the two perpendicular polarizations, as shown by the waveform and its Fourier transform (spectrum) in Figure 6. Transmission performance of the vortex generators designed for maximum T at 0.78 THz is

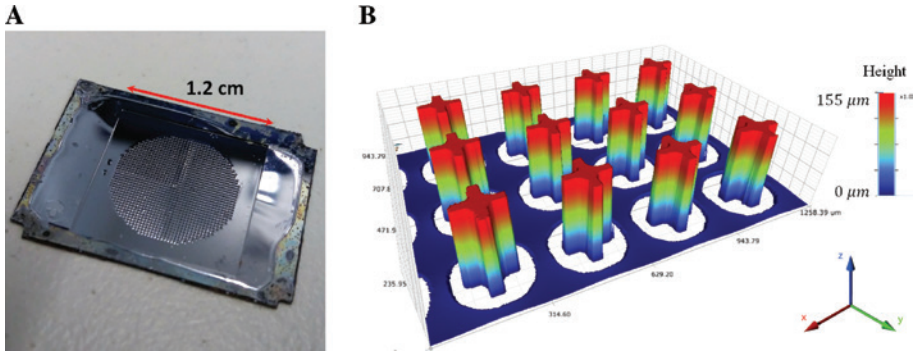

Figure 5: THz vortex generator and the height profile of the cross resonators measured using optical profiler.
(A) Photo of the fabricated metadevice for vortex beam generation. (B) Depth profile measured using an optical profilometer (Bruker).

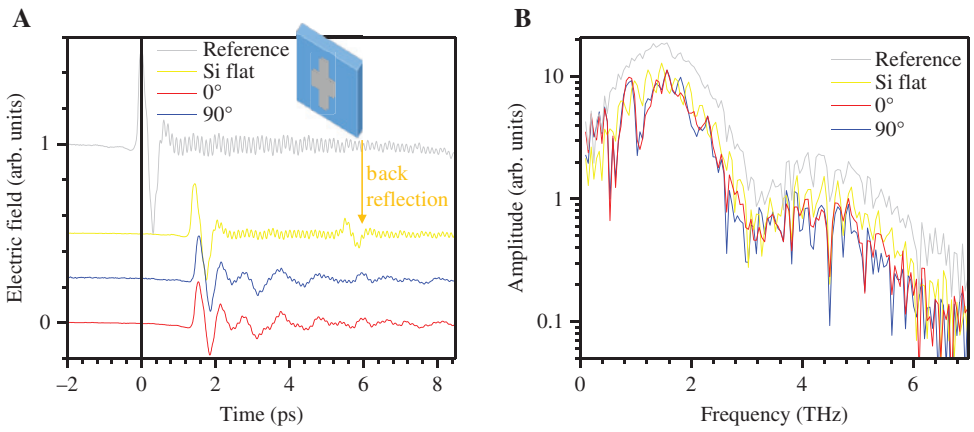

Figure 6: Polarization-independent action of the Si metasurface vortex generator measured by THz time-domain spectroscopy (THz-TDS). (A) Electric field transients (waveforms). Reference is the reflection signal from the GaAs antennae. Back-side reflection is shown on the waveform from the flat Si. Two perpendicular polarizations at 0° and 90° shows nearly identical waveforms. The high-frequency fringing is the result of the Fabri-Perot etalon made of the front and back surfaces of Si. (B) Fourier transform of the waveforms shown in (A).

shown in Figure 7. Closely matched spectral performance for two perpendicular polarizations was observed with the transmittance maximum at a slightly shifted 0.8 THz wavelength. The deviation is due to the slight mismatch between the simulated and fabricated dimensions of the cross-resonator.

The pattern of cross-antennas is also performing as a spectral filter. A promising application is to combine filtering and focusing by a flat Fresnel lens pattern to increase the signal-to-noise ratio in optical filtering as was recently demonstrated by laser ablation [40].

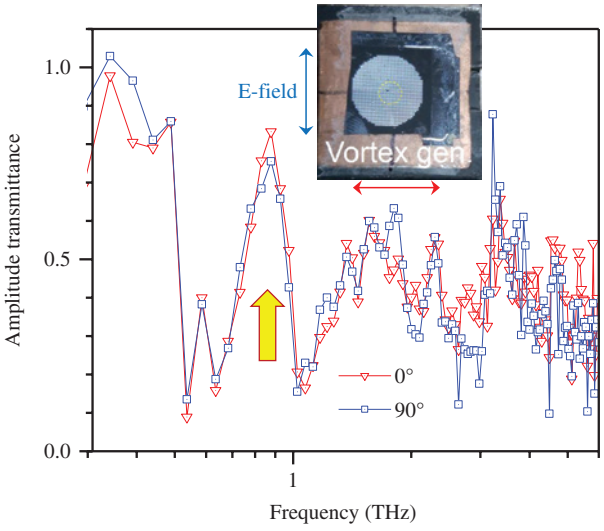

Figure 7: Transmission of the Si metasurface vortex generator. The peak is at 0.83 THz (arrow marker), which is close the designed 0.78 THz. The deviation is due to the slight mismatch between the simulated and fabricated dimensions of the cross-resonator.

3 Conclusions

Metasurfaces composed of azimutally rotated sections of cross-antennas patterned at different cross-lengths L and fixed period Λ were used to fabricate optical vortex generators. By using Si, we demonstrated that high-transmission optical elements at the designed wavelengths in mid-IR and THz spectral ranges could be made. The high refractive index of Si is beneficial for the required overlap of electric and magnetic resonances for the cross-antennas used in this work. The used cross-antenna design is beneficial for polarization-insensitive performance of the vortex beam generators. This is a useful virtue for synchrotron applications where the beam has a complex polarization composition [41].

This study shows that a missing toolbox of optical elements imparting OAM on to beams at IR spectral ranges is readily available using the metasurface approach. We used a linear scaling approach to demonstrate the vortex generator at THz wavelength and experimentally demonstrated the high transmission and polarization-independent behavior. Simulation results showed the desired spatial phase variability needed for beam-shaping applications.

Acknowledgments: The FPA-FTIR imaging experiment was carried out on the offline FTIR instrument at the Australian Synchrotron IRM Beamline, part of ANSTO, during the approved beamtime for Proposal ID M13416. This work was performed in part at the Melbourne Centre for Nanofabrication (MCN) in the Victorian Node of the Australian National Fabrication Facility (ANFF). This research was partially funded by JSPS KAKENHI. A.K. is grateful for support via the Russian Science Foundation

(grant no. 18-79-10091), and R.D. thanks the IIT Madras–Swinburne joint PhD program.

References

[1] Jansen C, Wietzke S, Peters O, et al. Terahertz imaging: applications and perspectives. Appl Opt 2010;49:E48–57.

[2] Redo-Sanchez A, Zhang X-C. Terahertz science and technology trends. IEEE J Sel Topics Quantum Electron 2008;14:260–9.

[3] Bitzer A, Walther M. Terahertz near-field imaging of metallic subwavelength holes and hole arrays. Appl Phys Lett 2008;92:231101.

[4] Honda R, Ryu M, Balčytis A, et al. Paracetamol micro-structure analysis by optical mapping. Appl Surf Sci 2019;473:127–32.

[5] Honda R, Ryu M, Li J-L, Mizeikis V, Juodkazis S, Morikawa J. Simple multi-wavelength imaging of birefringence: case study of silk. Sci Rep 2018;8:17652.

[6] Tonouchi M. Cutting-edge terahertz technology. Nat Photon 2007;1:97.

[7] Mittleman D. Sensing with terahertz radiation, vol. 85. Berlin, Heidelberg, Springer-Verlag, 2013.

[8] Wei X, Liu C, Niu L, et al. Generation of arbitrary order bessel beams via 3d printed axicons at the terahertz frequency range. Appl Opt 2015;54:10641–9.

[9] Liu C, Niu L, Wang K, Liu J. 3d-Printed diffractive elements induced accelerating terahertz airy beam. Opt Express 2016;24:29342–8.

[10] Machado F, Zagrajek P, Ferrando V, Monsoriu JA, Furlan WD. Multiplexing the vortex beams with a single diffractive 3-d printed lens. IEEE Trans Terahertz Sci Technol 2019;9:63–6.

[11] Nye JF, Berry MV. Dislocations in wave trains. Proc R Soc London A Math Phys Sci 1974;336:165–90.

[12] Barnett SM, Allen L. Orbital angular momentum and nonparaxial light beams. Opt Commun 1994;110:670–8.

[13] Srinivas P, Perumangatt C, Lal N, Singh R, Srinivasan B. Investigation of propagation dynamics of truncated vector vortex beams. Opt Lett 2018;43:2579–82.

[14] He H, Friese M, Heckenberg N, Rubinsztein-Dunlop H. Direct observation of transfer of angular momentum to absorptive particles from a laser beam with a phase singularity. Phys Rev Lett 1995;75:826.

[15] Ng J, Lin Z, Chan C. Theory of optical trapping by an optical vortex beam. Phys Rev Lett 2010;104:103601.

[16] Willner AE, Huang H, Yan Y, et al. Optical communications using orbital angular momentum beams. Adv Opt Photon 2015;7:66–106.

[17] Willig KI, Rizzoli SO, Westphal V, Jahn R, Hell SW. Sted microscopy reveals that synaptotagmin remains clustered after synaptic vesicle exocytosis. Nature 2006;440:935.

[18] Heckenberg N, McDuff R, Smith C, White A. Generation of optical phase singularities by computer-generated holograms. Opt Lett 1992;17:221–3.

[19] Matsumoto N, Ando T, Inoue T, Ohtake Y, Fukuchi N, Hara T. Generation of high-quality higher-order laguerre-gaussian beams using liquid-crystal-on-silicon spatial light modulators. J Opt Soc Am A 2008;25:1642–51.

[20] Beijersbergen M, Coerwinkel R, Kristensen M, Woerdman J. Helical-wavefront laser beams produced with a spiral phaseplate. Opt Commun 1994;112:321–7.

[21] Genevet P, Yu N, Aieta F, et al. Ultra-thin plasmonic optical vortex plate based on phase discontinuities. Appl Phys Lett 2012;100:013101.

[22] Hu D, Wang X, Feng S, et al. Ultrathin terahertz planar elements. Adv Opt Mater 2013;1:186–91.

[23] He J, Wang X, Hu D, Ye J, Feng S, Kan Q. Generation and evolution of the terahertz vortex beam. Opt Express 2013;21:20230–9.

[24] Devlin RC, Ambrosio A, Rubin NA, Mueller JB, Capasso F. Arbitrary spin-to–orbital angular momentum conversion of light. Science 2017;358:896–901.

[25] Yue F, Wen D, Xin J, Gerardot BD, Li J, Chen X. Vector vortex beam generation with a single plasmonic metasurface. ACS Photon 2016;3:1558–63.

[26] Yan C, Li X, Pu M, et al. Generation of polarization-sensitive modulated optical vortices with all-dielectric metasurfaces. ACS Photon 2019;6:628–33.

[27] Xiao S, Wang J, Liu F, Zhang S, Yin X, Li J. Spin-dependent optics with metasurfaces. Nanophotonics 2016;6:215–34.

[28] Kildishev AV, Boltasseva A, Shalaev VM. Planar photonics with metasurfaces. Science 2013;339:1232009.

[29] Chong KE, Staude I, James A, et al. Polarization-independent silicon metadevices for efficient optical wavefront control. Nano Lett 2015;15:5369–74.

[30] Khorasaninejad M, Chen WT, Devlin RC, Oh J, Zhu AY, Capasso F. Metalenses at visible wavelengths: diffraction-limited focusing and subwavelength resolution imaging. Science 2016;352:1190–4.

[31] Dharmavarapu R, Ng SH, Bhattacharya S, Juodkazis S. All-dielectric metasurface for wavefront control at terahertz frequencies. In: Nanophotonics Australasia 2017, vol. 10456, International Society for Optics and Photonics, SPIE conference proceeding: https://doi.org/10.1117/12.2283090, 2018: p. 104561W.

[32] Balčytis A, Ryu M, Wang X, et al. Silk: optical properties over 12.6 octaves THz-IR-Visible-UV range. Materials 2017;10:356.

[33] Ryu M, Kobayashi H, Balčytis A, et al. Nanoscale chemical mapping of laser-solubilized silk. Mater Res Express 2017;4:115028.

[34] Ryu M, Balčytis A, Wang X, et al. Orientational mapping augmented sub-wavelength hyper-spectral imaging of silk. Sci Rep 2017;7:7419.

[35] Ryu M, Honda R, Cernescu A, et al. Nanoscale optical and structural characterisation of silk. Beilstein J Nanotechnol 2019;10:922–9.

[36] Evlyukhin AB, Reinhardt C, Seidel A, Luk'yanchuk BS, Chichkov BN. Optical response features of si-nanoparticle arrays. Phys Rev B 2010;82:045404.

[37] Decker M, Staude I, Falkner M, et al. High-efficiency dielectric huygens' surfaces. Adv Opt Mater 2015;3:813–20.

[38] Dharmavarapu R, Bhattacharya S, Juodkazis S. MetaOptics: Software for creating GDSII layouts of metasurface phase masks. Available at: http://www.ee.iitm.ac.in/AppliedOptics/MetaOptics.exe. Accessed: 1 Apr 2019.

[39] Yokota K, Takeda J, Dang C, et al. Surface metallic states in ultrathin Bi(001) films studied with terahertz time-domain spectroscopy. Appl Phys Lett 2012;100:251605.

[40] Tamošiūnaitė M, Indrišiūnas S, Tamošiūnas V, et al. Focusing of terahertz radiation with laser-ablated antireflective structures. IEEE Trans Terahertz Sci Technol 2018;8:541–8.

[41] Ryu M, Linklater D, Hart W, et al. 3D printed polarising grids for IR-THz synchrotron radiation. J Opt 2018;20:035101.